Upscattered Cocoon Emission in Short Gamma-Ray Bursts as High-energy Gamma-Ray Counterparts to Gravitational Waves

Shigeo S. Kimura[1,2,3,4,5] , Kohta Murase[3,4,5,6] , Kunihito Ioka[6] , Shota Kisaka[1,2], Ke Fang[7,8] , and Peter Mészáros[3,4,5]

[1] Frontier Research Institute for Interdisciplinary Sciences, Tohoku University, Sendai 980-8578, Japan
[2] Astronomical Institute, Tohoku University, Sendai 980-8578, Japan
[3] Department of Physics, Pennsylvania State University, University Park, PA 16802, USA
[4] Department of Astronomy & Astrophysics, Pennsylvania State University, University Park, PA 16802, USA
[5] Center for Particle and Gravitational Astrophysics, Pennsylvania State University, University Park, PA 16802, USA
[6] Center for Gravitational Physics, Yukawa Institute for Theoretical Physics, Kyoto, Kyoto 606-8502, Japan
[7] Kavli Institute for Particle Astrophysics and Cosmology (KIPAC), Stanford University, Stanford, CA 94305, USA

Abstract

We investigate prolonged engine activities of short gamma-ray bursts (SGRBs), such as extended and/or plateau emissions, as high-energy gamma-ray counterparts to gravitational waves (GWs). Binary neutron-star mergers lead to relativistic jets and merger ejecta with r-process nucleosynthesis, which are observed as SGRBs and kilonovae/macronovae, respectively. Long-term relativistic jets may be launched by the merger remnant as hinted in X-ray light curves of some SGRBs. The prolonged jets may dissipate their kinetic energy within the radius of the cocoon formed by the jet–ejecta interaction. Then the cocoon supplies seed photons to nonthermal electrons accelerated at the dissipation region, causing high-energy gamma-ray production through the inverse Compton scattering process. We numerically calculate high-energy gamma-ray spectra in such a system using a one-zone and steady-state approximation, and show that GeV–TeV gamma-rays are produced with a duration of 10^2–10^5 s. They can be detected by *Fermi*/LAT or CTA as gamma-ray counterparts to GWs.

Unified Astronomy Thesaurus concepts: High energy astrophysics (739); Gamma-ray bursts (629); Gamma-ray astronomy (628); Gravitational wave astronomy (675); Gamma-ray transient sources (1853); Non-thermal radiation sources (1119); Relativistic jets (1390)

1. Introduction

The first binary neutron star (BNS) merger event, GW170817, was initially detected by the gravitational waves (GWs; Abbott et al. 2017b, 2017c). About two seconds later, *Fermi*/GBM and *INTEGRAL*/SPI-ACS detected the gamma-ray counterpart, which supports the BNS merger paradigm as the progenitor of short gamma-ray bursts (SGRBs; Abbott et al. 2017a). The time lag may imply that the jet launch is delayed for ~1 s (e.g., Gottlieb et al. 2018b; Zhang 2019), although other mechanisms can cause time delay (e.g., Ioka & Nakamura 2018; Shoemaker & Murase 2018). The broadband counterparts also confirmed the existence of a relativistic jet (e.g., Mooley et al. 2018a, 2018b; Troja et al. 2018a; Ghirlanda et al. 2019; Lamb et al. 2019a), which is consistent with an SGRB observed from an off-axis angle (e.g., Ioka & Nakamura 2018, 2019; Troja et al. 2018b). The UV/optical/IR counterparts (Coulter et al. 2017; Lipunov et al. 2017; Evans et al. 2017; Pian et al. 2017; Smartt et al. 2017; Soares-Santos et al. 2017; Tanvir et al. 2017; Utsumi et al. 2017; Valenti et al. 2017) also verified that a BNS merger produces fast and massive ejecta consisting of r-process elements (e.g., Kasliwal et al. 2017; Kasen et al. 2017; Murguia-Berthier et al. 2017; Shibata et al. 2017; Tanaka et al. 2017). Gamma-rays above GeV energies and neutrinos are not detected from GW170817 (Abdalla et al. 2017; Albert et al. 2017; Ajello et al. 2018), although they are expected (e.g., Gao et al. 2013; Fang & Metzger 2017; Kimura et al. 2017, 2018; Murase et al. 2018).

Light curves of X-ray observations of classical SGRBs have rapidly declining or variable components, such as extended or

plateau emissions (Norris & Bonnell 2006; Sakamoto et al. 2011; Kagawa et al. 2015, 2019; Kaneko et al. 2015), which are interpreted as prolonged activities of either a magnetar or a black hole (Ioka et al. 2005; Perna et al. 2006; Metzger et al. 2008; Rowlinson et al. 2013; Gompertz et al. 2014; Kisaka & Ioka 2015; Kisaka et al. 2017). Since the duration of the prolonged activities is about 10^2–10^5 s, it may be feasible to detect other counterparts of such prolonged emissions with current and near future facilities. However, characteristics of the prolonged jets have yet to be determined.

In this Letter, we discuss the upscattered cocoon photons as GeV–TeV counterparts to GWs to probe the prolonged jets. Along this line, Murase et al. (2018) and Veres & Mészáros (2014) proposed using GeV–TeV gamma-ray emissions to probe the prolonged dissipation in SGRB jets, in which interactions between prolonged X-rays and electrons accelerated at external shocks were considered. We here consider primary electron acceleration associated with the late dissipation itself (e.g., Ghisellini et al. 2007; Murase et al. 2011). If the ejecta is produced before the jet launch, the jet–ejecta interaction forms a cocoon surrounding the jet (e.g., Mészáros & Rees 2001; Ramirez-Ruiz et al. 2002; Bromberg et al. 2011; Mizuta & Ioka 2013; Nagakura et al. 2014; Lazzati et al. 2017; Gottlieb et al. 2018a; Hamidani et al. 2019). Since the cocoon freely expands after it breaks out from the ejecta, the dissipation of the prolonged jets may occur inside the cocoon (Kisaka et al. 2015, 2017). The cocoon supplies a large amount of photons to the dissipation region, which are upscattered by nonthermal electrons accelerated there (see Figure 1). The upscattered photons interact with the cocoon photons before they escape from the system, which initiates electromagnetic
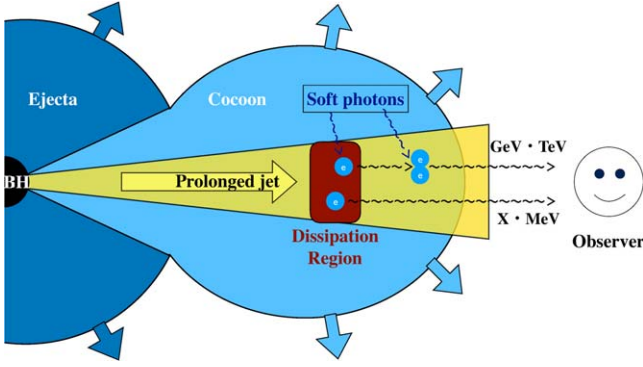
---

[8] Einstein Fellow.

Figure 1. Schematic picture of our model. The prolonged jet dissipates its kinetic energy within the cocoon radius. The cocoon supplies soft photons to the dissipation region, leading to GeV–TeV gamma-ray production through the EIC process. Higher-energy gamma-rays are attenuated and reprocessed to lower energies by the cocoon photons before escaping from the system.

cascades. We calculate the spectrum of GeV–TeV gamma-rays escaping from such a system, and discuss the prospects for future detection as gamma-ray counterparts to GWs. Such an external inverse Compton scattering (EIC) process using the cocoon photons is discussed by Toma et al. (2009). They considered the prompt jets with energy dissipation outside the cocoon radius, while we focus on the prolonged jets with energy dissipation inside the cocoon radius with a more realistic setup.

We use the notation $Q_X = Q/10^X$ in cgs unit unless otherwise noted and write Q' for the physical quantities in the comoving frame.

2. The Cocoon

We estimate the physical quantities of the cocoon in the engine frame. Based on the hydrodynamic simulations of the jet propagation in the ejecta (Hamidani et al. 2019; H. Hamidani et al. 2019, in preparation), we set the cocoon mass and average velocity to be $M_{\rm coc} \sim 10^{-4}\,M_\odot$ and $\beta_{\rm coc} \sim 0.32$. These values are not so sensitive to the jet luminosity. The kinetic energy of the cocoon is estimated to be $\mathcal{E}_{k,\rm coc} \approx M_{\rm coc}\beta_{\rm coc}^2 c^2/2 \sim 8.9 \times 10^{48} M_{\rm coc,-4}\beta_{\rm coc,-0.5}^2$ erg, where $M_{\rm coc,-4} = M_{\rm coc}/(10^{-4}\,M_\odot)$.

The thermal energy of the cocoon is initially deposited by the jet–ejecta interaction. Following the simulations by H. Hamidani et al. (2019, in preparation), we set the initial thermal energy of the cocoon to be a fifth of its kinetic energy: $\mathcal{E}_{\rm ini} \approx \mathcal{E}_{k,\rm coc}/5 \approx 1.8 \times 10^{48}$ erg. For bright prompt jets of SGRBs, the velocity of the jet head is approximated to be $\beta_h \sim 1$. Then, the breakout time of the prompt jet is estimated to be $t_{\rm bo} \approx \beta_{\rm ej}t_{\rm lag}/(\beta_h - \beta_{\rm ej}) \simeq 0.25t_{\rm lag,0}$ (Murguia-Berthier et al. 2014; Matsumoto & Kimura 2018; Hamidani et al. 2019), where $t_{\rm lag} \sim 1$ s is the lag time between the merger and jet launch. After the breakout, the cocoon loses its internal energy by adiabatic expansion. We can obtain the internal energy as $\mathcal{E}_{\rm ad} \approx \mathcal{E}_{\rm ini}(R_{\rm bo}/R_{\rm coc}) \simeq 2.8 \times 10^{43}\beta_{\rm coc,-0.5}t_{\rm dur,4}^{-1}$ erg, where $R_{\rm bo} \approx t_{\rm bo}\beta_{\rm ej}c \sim 1.5 \times 10^9$ cm is the ejecta radius when the prompt jet breaks out ($\beta_{\rm ej} \approx 0.2$ is the ejecta velocity), $R_{\rm coc} \approx t_{\rm dur}\beta_{\rm coc}c \sim 9.5 \times 10^{13}t_{\rm dur,4}\beta_{\rm coc,-0.5}$ cm is the cocoon radius ($t_{\rm dur}$ is the time after the merger). The radioactive decay of r-process elements also heats up the cocoon. The specific heating rate by the decay chain is expressed by a power-law function for $t_{\rm dur} > 1$ s; $\dot{\varepsilon}_{\rm ra} \approx 1.6 \times 10^{11}t_{\rm dur,4}^{-1.3}$ erg g^{-1} s^{-1}

(Korobkin et al. 2012; Hotokezaka et al. 2016). The balance between the adiabatic cooling and radioactive heating provides the internal energy to be $\mathcal{E}_{\rm ra} \approx \dot{\varepsilon}_{\rm ra}M_{\rm coc}t_{\rm dur} \simeq 3.3 \times 10^{44}t_{\rm dur,4}^{-0.3}M_{\rm coc,-4}$ erg. We write down the cocoon internal energy as $\mathcal{E}_{\rm coc} \approx \mathcal{E}_{\rm ad} + \mathcal{E}_{\rm ra}$. The radioactive heating is the dominant process for $t_{\rm dur} > 300$ s with our reference parameter set.

The optical depth of the cocoon is estimated to be $\tau_{\rm coc} \approx 3\kappa_{\rm coc}M_{\rm coc}/(4\pi R_{\rm coc}^2) \simeq 53\kappa_{\rm coc,1}M_{\rm coc,-4}\beta_{\rm coc,-0.5}^{-2}t_{\rm dur,4}^{-2}$, where $\kappa_{\rm coc} \sim 10$ cm^2 g^{-1} is the opacity by r-process elements. Hence, the photons inside the cocoon should be thermalized. The temperature of the cocoon is written as $a_{\rm rad}T_{\rm coc}^4 \approx 3\mathcal{E}_{\rm coc}/(4\pi R_{\rm coc}^3)$, where $a_{\rm rad}$ is the radiation constant. Also, the high optical depth allows us to ignore the photon diffusion effect when estimating the internal energy of the cocoon. Note that the opacity and heating rate in the cocoon may be lower because the neutrino irradiation by the remnant neutron star reduces the amount of lanthanide elements (Fujibayashi et al. 2018; Metzger et al. 2018).

3. Nonthermal Electrons

We consider a prolonged jet with Lorentz factor Γ_j, isotropic-equivalent kinetic luminosity $L_{k,\rm iso}$, and duration $t_{\rm dur}$. The jet dissipates its kinetic energy at radius $R_{\rm dis}$ through some mechanisms, such as internal shocks (Rees & Meszaros 1994) or magnetic reconnections (McKinney & Uzdensky 2012). The electron luminosity is set to be $L_{e,\rm iso} = \epsilon_e L_{k,\rm iso}$, leading to the comoving isotropic-equivalent electron luminosity of $L'_{e,\rm iso} \approx L_{e,\rm iso}/\Gamma_j^2$. The comoving magnetic field energy density is given as $U'_B = \epsilon_B L_{k,\rm iso}/(4\pi R_{\rm dis}^2\Gamma_j^2 c)$, and the comoving magnetic field is $B' = \sqrt{8\pi U'_B}$. The electron acceleration via diffusive shock acceleration requires the shock upstream region to be optically thin (Murase & Ioka 2013; Kimura et al. 2018). The optical depth is estimated to be $\tau_j \approx n'_j\sigma_T R_{\rm dis}/\Gamma_j \simeq 3.7 \times 10^{-4}L_{k,\rm iso,48.5}R_{\rm dis,13}^{-1}\Gamma_{j,2}^{-3}$, where $n'_j = L_{k,\rm iso}/(4\pi R_{\rm dis}^2\Gamma_j^2 m_p c^3)$ is the comoving number density and σ_T is the Thomson cross section. Hence, the electrons can be accelerated in a jet of $L_{k,\rm iso} \lesssim 10^{51}$ erg s^{-1} and $\Gamma_j \gtrsim 100$. The lateral optical depth is estimated to be $\tau_\theta \approx \tau_j\theta_j\Gamma_j \simeq 3.7 \times 10^{-3}L_{k,\rm iso,48.5}R_{\rm dis,13}^{-1}\Gamma_{j,2}^{-2}\theta_{j,-1}$, where θ_j is the jet opening angle. Thus, the cocoon photons can diffuse into the internal dissipation region as long as the opening angle is small enough.

The electron distribution in the comoving frame is given by the transport equation that includes injection, cooling, and adiabatic loss terms. Assuming the steady state, the transport equation is written as

$$\frac{d}{d\gamma'_e}\left(-\frac{\gamma'_e}{t'_{\rm cool}}N_{\gamma'_e}\right) = \dot{N}_{\gamma'_e,\rm inj} - \frac{N_{\gamma'_e}}{t'_{\rm dyn}}, \quad (1)$$

where γ'_e is the electron Lorentz factor, $N_{\gamma'_e} = dN/d\gamma'_e$ is the number spectrum, $t'_{\rm cool}$ is the cooling time, $\dot{N}_{\gamma'_e,\rm inj}$ is the injection term, and $t'_{\rm dyn} = R_{\rm dis}/(\Gamma_j c)$ is the dynamical time. A solution of this equation is given in Equation (C.11) of Dermer & Menon (2009), and we numerically integrate the solution. Note that the cooling timescale depends on the photon density that is affected by the electron distribution. We iteratively calculate the electron distribution until the solution converges (see Murase et al. 2011).
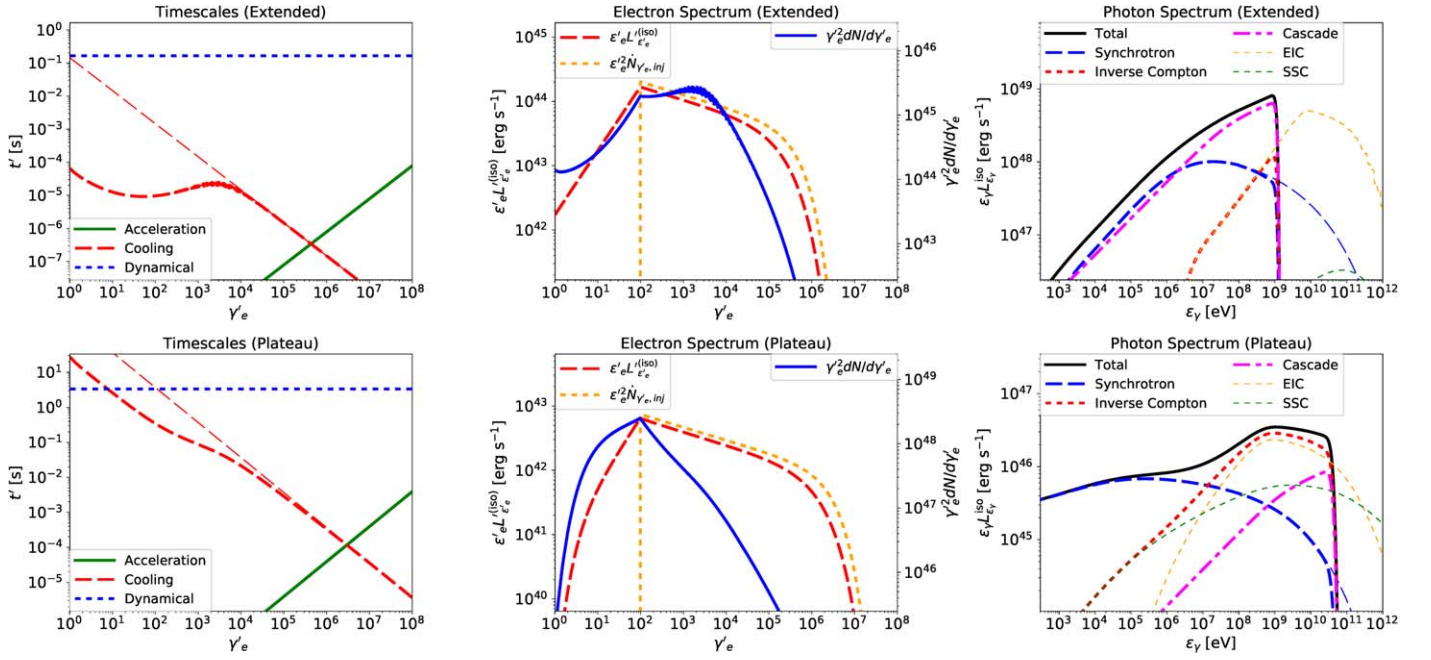
Figure 2. Timescales in the comoving frame (left), electron spectrum at the dissipation region in the comoving frame (middle), and photon spectrum in the engine frame (right) for models of extended (top) and plateau (bottom) emissions. In the left column, the dashed, dotted, and solid lines show the cooling, dynamical, and acceleration timescales. The thin dashed line is the synchrotron cooling timescale, while the thick-dashed line is the total cooling timescale. In the middle column, the solid, dotted, and dashed lines depict the number spectrum, the injection spectrum, and the differential electron luminosity. In the right column, the thick and thin lines are for the escape and intrinsic photon spectra. We plot the attenuated total (solid-black), attenuated and intrinsic synchrotron (blue dashed), cascade (magenta dotted–dashed), attenuated SSC + EIC (red dotted), intrinsic EIC (orange dotted), and intrinsic SSC (green dotted) spectra.

We write the injection term as a power-law function with an exponential cutoff:

$$\dot{N}_{\gamma'_e,\mathrm{inj}} = \dot{N}_{\mathrm{nor}}\left(\frac{\gamma'_e}{\gamma'_{e,\mathrm{cut}}}\right)^{-p_{\mathrm{inj}}}\exp\left(-\frac{\gamma'_e}{\gamma'_{e,\mathrm{cut}}}\right), \tag{2}$$

where $\dot{N}_{\mathrm{nor}}$ is the normalization factor and $\gamma'_{e,\mathrm{cut}}$ is the cutoff energy. The normalization is determined so that $\int \dot{N}_{\gamma'_e,\mathrm{inj}}\gamma'_e m_e c^2 d\gamma'_e = L'_{e,\mathrm{iso}}$ is satisfied. The cutoff energy is given by balance between the acceleration and cooling timescales. We estimate the acceleration time to be $t'_{\mathrm{acc}} \approx \gamma'_e m_e c/(eB')$. As the cooling processes, we consider the synchrotron, synchrotron-self Compton (SSC), and EIC processes. The synchrotron cooling timescale is estimated to be $t'_{\mathrm{syn}} = 6\pi m_e c/(\gamma'_e \sigma_T B'^2)$. The inverse Compton cooling rate is written in Equations (2.48) and (2.56) in Blumenthal & Gould (1970). We write the differential energy density of seed photons for SSC as

$$U'^{(\mathrm{ssc})}_{\bar{\varepsilon}'_\gamma} = \frac{L'^{(\mathrm{syn})}_{\bar{\varepsilon}'_\gamma}}{4\pi R^2_{\mathrm{dis}} c}, \tag{3}$$

where $\bar{\varepsilon}'_\gamma$ is the seed photon energy and $L'^{(\mathrm{syn})}_{\bar{\varepsilon}'_\gamma}$ is the synchrotron differential luminosity (see Section 4). The seed photons for EIC are the thermal photons in the cocoon boosted by the jet's relativistic motion:

$$U'^{(\mathrm{eic})}_{\bar{\varepsilon}'_\gamma} = \Gamma_j \frac{8\pi(\bar{\varepsilon}'_\gamma/\Gamma_j)^3}{h^3 c^3}\frac{1}{\exp\left(\frac{\bar{\varepsilon}'_\gamma/\Gamma_j}{k_B T_{\mathrm{coc}}}\right) - 1}. \tag{4}$$

In reality, the photon density and photon temperature in the jet may be slightly lower than those in the cocoon, but we use the photon field in the cocoon for simplicity. This does not strongly affect our results as long as the jet is well collimated and filled with thermal photons.

The left column of Figure 2 shows the cooling and acceleration timescales for models of a typical extended emission (EE) and plateau emission (PE), whose parameters and resulting quantities are tabulated in Tables 1 and 2. Note that we here assume a small R_{dis} compared to the previous works (e.g., Toma et al. 2009; Kimura et al. 2017) such that $R_{\mathrm{dis}} < R_{\mathrm{coc}}$ is satisfied. For the EE model, the EIC dominates over the other loss processes for $\gamma'_e \lesssim 3 \times 10^3$, while the synchrotron is the most efficient above it due to strong Klein–Nishina (KN) suppression. For the PE model, the adiabatic loss is dominant for $\gamma'_e \lesssim 10$, EIC is efficient for $10 < \gamma'_e < 6 \times 10^3$, and synchrotron loss is relevant above it.

The resulting electron spectra are shown in the middle column of Figure 2. For the EE model, the electron number spectrum, $\gamma'^2_e dN/d\gamma'_e$, shows a hardening for $\gamma'_e \lesssim 3 \times 10^3$ due to the KN effect. For the PE model, the electron spectrum is peaky because of the adiabatic loss below the injection Lorentz factor and the cooling break above it. The cutoff energies are $\gamma'_{e,\mathrm{cut}} \sim 4 \times 10^5$ and 3×10^6 for the EE and PE models, respectively. We also plot $\varepsilon'_e L'^{(\mathrm{iso})}_{\varepsilon'_e} = \gamma'^2_e m_e c^2 (dN/d\gamma'_e) t'^{-1}_{\mathrm{cool}}$ and $\dot{N}_{\gamma'_e,\mathrm{inj}}$ in the figure. The two spectra are almost identical for $\gamma'_e > \gamma'_m$, which confirms the convergence of the numerical integration and iteration.

Table 1
Values of the Fixed Parameters

$M_{\rm coc}$ ($M_\odot$)	$\beta_{\rm coc}$	$R_{\rm bo}$ (cm)	ϵ_B	ϵ_e	$p_{\rm inj}$	γ_m
10^{-4}	0.32	1.5×10^9	0.01	0.1	2.2	100

4. Gamma-Ray Spectra

We numerically calculate photon spectra emitted by the nonthermal electrons. For the synchrotron differential luminosity, we use the formula given by Equations (18)–(20) in Finke et al. (2008). The spectrum by the inverse Compton scattering is written in Equations (2.48) and (2.61) in Blumenthal & Gould (1970), and the seed photon densities for SSC and EIC are given by Equations (3) and (4), respectively.

Gamma-rays can be attenuated through $\gamma\gamma$ annihilation inside the system. With our reference parameter sets, the attenuation at the dissipation region is negligible, while the attenuation within the cocoon radius is relevant. Using the quantities in the engine frame, the optical depth for $\gamma\gamma$ interaction is represented by

$$\tau_{\gamma\gamma}(\varepsilon_\gamma) \approx (R_{\rm coc} - R_{\rm dis}) \int \mathscr{R}(x) \frac{U_{\overline{\varepsilon}_\gamma}}{\overline{\varepsilon}_\gamma} d\overline{\varepsilon}_\gamma, \tag{5}$$

where ε_γ is the gamma-ray energy, $\overline{\varepsilon}_\gamma$ is the soft photon energy in the cocoon, $x = \varepsilon_\gamma \overline{\varepsilon}_\gamma/(m_e c^2)$, $\mathscr{R}(x)$ is given in Equation (4.7) in Coppi & Blandford (1990), and $U_{\overline{\varepsilon}_\gamma}$ is the thermal photon energy density in the cocoon. Note that we focus on the situation where $R_{\rm coc} > R_{\rm dis}$ (see Figure 1). The optical depth above $\sim$1 GeV (100 GeV) for EE (PE) model is very high, so an electromagnetic cascade is initiated. We approximately calculate the cascade spectrum following Zdziarski (1988). The cascade spectrum is approximated to be

$$\varepsilon_\gamma L_{\varepsilon_\gamma}^{\rm (cas)} \approx \varepsilon_\gamma G(y) \tag{6}$$

$$G(y) = \frac{L_{\rm nor}}{\varepsilon_{\gamma,\rm cut}}(y^{3.2} + y^2)^{-1/4} \exp(-\tau_{\gamma\gamma}), \tag{7}$$

where $L_{\rm nor}$ is the normalization factor, $\varepsilon_{\gamma,\rm cut}$ is the cutoff energy above which $\tau_{\gamma\gamma} > 1$ is satisfied, and $y = \varepsilon_\gamma/\varepsilon_{\gamma,\rm cut}$ (see also Murase et al. 2012). $G(y)$ is normalized so that the luminosity of the cascade emission is equal to the energy loss rate by the attenuation.

The calculated photon spectra in the engine frame are shown in the right column of Figure 2. For the EE model, the injected electrons upscatter the seed photons in the KN regime, so that the EIC process produces high-energy gamma-rays of $\Gamma_j \gamma'_m m_e c^2 \simeq 10$ GeV. These gamma-rays are absorbed within the cocoon radius and reprocessed as the cascade emission, which is dominant for $\varepsilon_\gamma \gtrsim 1$ MeV in the escaping photon spectrum. The synchrotron emission provides a dominant contribution below it with a hard spectrum. The peak of the synchrotron emission is around 10 MeV due to the strong magnetic field (see Table 2) and the hard electron distribution. From the observations, the mean value of the photon indices for EEs in the Swift/XRT band is 1.7 (Kagawa et al. 2019), which is close to our results of 1.5. For the PE model, the injection energy is in the Thomson regime, and the EIC process produces photons of $\varepsilon_\gamma \gtrsim 4\Gamma_j^2 \gamma'_m{}^2 k_B T_{\rm coc} \sim 0.4$ GeV. Above

$\varepsilon_\gamma \gtrsim (m_e c^2)^2/(3k_B T_{\rm coc}) \sim 100$ GeV, the KN suppression is effective. The synchrotron emission produces photons below 20 MeV with a spectral index close to 2, which is also consistent with the observed spectra (Kagawa et al. 2019). The cascade and SSC emissions are subdominant. Note that the cutoff energy of the escaping photon spectrum is independent of the Lorentz factor of the jets as long as the electromagnetic cascades in the dissipation region are negligible. Using the cocoon temperature, we have $\varepsilon_{\gamma\gamma,\rm cut} \approx (m_e c^2)^2/(3k_B T_{\rm coc}) \simeq 4.6$ GeV and 95 GeV for the EE and PE model, respectively. In our cases this overestimates the cutoff energy by a factor of 2–5 because $\tau_{\gamma\gamma} > 1$ is satisfied at the exponential tail of the cocoon photons.

5. Detection Prospects

We calculate GeV–TeV gamma-ray fluxes from the prolonged jets with various $t_{\rm dur}$ and discuss future detection prospects. The observed EEs and PEs indicate a rough correlation between X-ray luminosity and duration: $L_{\rm XRT} \sim 10^{49}(t_{\rm dur}/10^2\,{\rm s})^{2.5}$ erg s^{-1} for the EE model and $L_{\rm XRT} \sim 10^{46}(t_{\rm dur}/10^4\,{\rm s})^2$ erg s^{-1} for the PE model, where $L_{\rm XRT}$ is the photon luminosity in 0.3–10 keV in the observer frame (Kisaka et al. 2017). By adjusting the value of $L_{k,\rm iso}$, we iteratively calculate the escaping photon spectra for various values of $t_{\rm dur}$ such that the resulting $L_{\rm XRT}$ satisfies the relation above. Here, the XRT band is converted to the engine frame using the mean redshift of the observed EEs, $z = 0.72$ (Kisaka et al. 2017). Our reference models are in rough agreement with the relation (see Table 2). We focus on 200 sec $< t_{\rm dur} < 4 \times 10^4$ s because $\tau_j > 0.3$ and $\tau_{\rm coc} < \beta_{\rm coc}$ are satisfied for $t_{\rm dur} < 200$ s and $t_{\rm dur} > 4 \times 10^4$ s, respectively, where our assumptions become inappropriate. Note that the relation between $L_{\rm XRT}$ and $t_{\rm dur}$ strongly depends on the sample and fitting formula (Dainotti et al. 2008, 2010; Kisaka et al. 2017; Kagawa et al. 2019).

In Figure 3, we show the gamma-ray fluxes on Earth in the Fermi/LAT and CTA bands for $d_L = 0.3$ Gpc ($z = 0.067$; thick line) and $d_L = 4.4$ Gpc ($z = 0.72$; thin line), which correspond to the GW detection horizon for the advanced LIGO design sensitivity and the average distance to SGRBs with EEs (Kisaka et al. 2017). The results are depicted as a function of the observed duration, $T_{\rm dur} = (1 + z)t_{\rm dur}$. We also plot the CTA sensitivity at 50 GeV (Cherenkov Telescope Array Consortium et al. 2019) and the upper limit for GW170817 by LAT (Ajello et al. 2018; Murase et al. 2018) that mimics the LAT sensitivity.

GeV gamma-ray emission expected in the EE model is so bright that LAT can easily detect the signals even for $d_L = 4.4$ Gpc. Indeed, LAT detected high-energy gamma-rays from two SGRBs, GRB 160702A and 170127C, about 1000 s after the trigger (Ajello et al. 2019), which could be explained by our model; though, detailed fits of individual bursts are beyond the scope of this paper. However, LAT has not detected any SGRBs with EEs in $T_{\rm dur} < 10^3$ s (Ajello et al. 2019), which seems in tension with our model. The cocoon may have a faster and hotter component in its outer region, depending on the initial configuration (Kyutoku et al. 2014; Kasliwal et al. 2017). The hot component will attenuate the high-energy gamma-rays. Also, if the dissipation region is outside the cocoon radius, which is likely to occur at early times, the EIC flux is significantly reduced. These effects need to be considered to

Table 2
Values of the Model Parameters and Physical Quantities

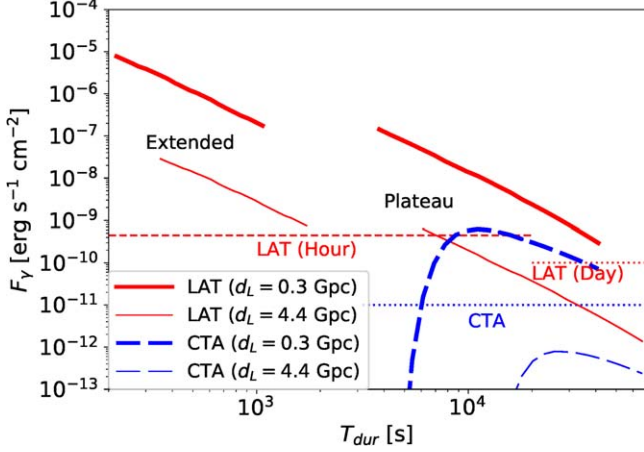| Model	Γ_j	$L_{k,\mathrm{iso}}$ (erg s^{-1})	R_{dis} (cm)	t_{dur} (s)	τ_{coc}	τ_j	R_{coc} (cm)	$k_B T_{\mathrm{coc}}$ (eV)	B' (G)	L_{XRT} (erg s^{-1})
Extended (EE)	200	$10^{50.5}$	10^{12}	$10^{2.5}$	5.3×10^4	4.6×10^{-2}	3.0×10^{12}	19	7.3×10^4	2.4×10^{47}
Plateau (PE)	100	$10^{48.5}$	10^{13}	10^4	53	3.7×10^{-4}	9.5×10^{13}	0.92	1.5×10^3	1.7×10^{46}

Figure 3. Gamma-ray fluxes in LAT (red solid) and CTA (blue dashed) bands. The thick and thin lines are for $d_L = 0.3$ Gpc and $d_L = 4.4$ Gpc, respectively. The red dashed and red dotted lines are the LAT upper limit for GW170817 with $\sim 10^3$ s integration (Ajello et al. 2018) and 1 day integration (Murase et al. 2018), respectively. The blue dotted line is the sensitivity of CTA for $\varepsilon_\gamma \simeq 50$ GeV for 5 hr integration (Cherenkov Telescope Array Consortium et al. 2019).

explain the nondetection by LAT, and a detailed study remains as a future work.

In contrast, the PE model is too faint to be detected by both CTA and LAT for $d_L = 4.4$ Gpc except for $T_{\mathrm{dur}} \lesssim 7 \times 10^3$ s by LAT. For $d_L = 0.3$ Gpc, LAT can detect the PEs for the range of durations we investigate here. CTA can also detect the PEs of $T_{\mathrm{dur}} < 6 \times 10^3$ s, although it cannot detect the PEs of shorter duration because of its high-energy threshold. Although we focus only on the case with $\tau_{\mathrm{coc}} > \beta_{\mathrm{coc}}$, the EIC emission may last longer, because the bulk of the merger ejecta (kilonova/macronova) continues to provide seed photons to the dissipation region.

6. Summary and Discussion

We have considered high-energy gamma-ray emission from prolonged engine activities in SGRBs. We assume that the prolonged jets dissipate their kinetic energy inside the cocoon radius, which provides nonthermal electrons in the dissipation region. The jet–ejecta interaction also produces copious thermal photons, leading to high-energy gamma-ray emission through the EIC process. The calculated photon spectrum is consistent with the X-ray observation, and LAT and CTA can detect gamma-ray counterparts to GWs for a duration of 10^2–10^5 s. Note that the counterparts by the prolonged engine activities may not be accompanied by the prompt gamma-rays as discussed in Xue et al. (2019) and Matsumoto & Kimura (2018). Also, *Fermi* and/or CTA may be able to detect the upscattered cocoon photons from the SGRBs that occur beyond the GW detection horizon. Hence, the follow-up observations should be performed for GWs without SGRBs and for SGRBs without GWs.

The afterglow and prompt gamma-ray emissions of GW170817 suggest that the jet is structured such that a fast core is surrounded by a slower wing (e.g., Lazzati et al. 2018; Lyman et al. 2018; Margutti et al. 2018; Xie et al. 2018; Ioka & Nakamura 2019). If the prolonged jet is structured, the kinetic luminosity at the edge needs to decrease faster than $L_{k,\mathrm{iso}} \propto \Gamma_j^{-2}$ in order to fill the jet core with the cocoon photons. The slower edge emits photons to a wider angle, which are reflected by the cocoon. Such photons will be detectable as a wide-angle counterpart to GWs (Kisaka et al. 2015, 2018). Note that the high-energy gamma-rays are not reflected but absorbed by the cocoon through the Bethe–Heitler pair-production process. Thus, LAT or Cerenkov Telescopes would have difficulty detecting the gamma-rays from off-axis events, including GW170817.

The prolonged jets may have a lower Lorentz factor (Lamb et al. 2019b; T. Matsumoto et al. 2019, in preparation). For the EE model with $\Gamma_j \lesssim 40$, $\tau_j > 1$ is satisfied, so the nonthermal particle acceleration does not occur. This condition can be avoided in the jet edge where a kinetic luminosity can be lower, although the emission from the jet edge cannot achieve the observed X-ray luminosity for EEs. For the EE model with $\Gamma_j \lesssim 100$, the GeV gamma-rays are attenuated in the dissipation region due to a higher photon density. In this case, if protons are accelerated simultaneously, high-energy neutrinos can be efficiently produced owing to the high target photon density, as has been discussed for X-ray flares and EEs of SGRBs (e.g., Murase & Nagataki 2006; Kimura et al. 2017). Such neutrinos would be detectable in the planned next-generation neutrino detector, IceCube-Gen2 (Aartsen et al. 2014). The detection of either high-energy gamma-rays or neutrinos will unravel the Lorentz factor and jet composition, or the nondetection will enable us to place a useful constraint on the emission radius.

ORCID iDs

Shigeo S. Kimura https://orcid.org/0000-0003-2579-7266
Kohta Murase https://orcid.org/0000-0002-5358-5642
Kunihito Ioka https://orcid.org/0000-0002-3517-1956
Ke Fang https://orcid.org/0000-0002-5387-8138
Peter Mészáros https://orcid.org/0000-0002-4132-1746

References

Aartsen, M. G., et al. 2014, arXiv:1412.5106

Abbott, B. P., Abbott, R., Abbott, T. D., et al. 2017a, ApJL, 848, L13
Abbott, B. P., Abbott, R., Abbott, T. D., et al. 2017b, PhRvL, 119, 161101
Abbott, B. P., Abbott, R., Abbott, T. D., et al. 2017c, ApJL, 848, L12
Abdalla, H., Abramowski, A., Aharonian, F., et al. 2017, ApJL, 850, L22
Ajello, M., Allafort, A., Axelsson, M., et al. 2018, ApJ, 861, 85
Ajello, M., Arimoto, M., Axelsson, M., et al. 2019, ApJ, 878, 52
Albert, A., André, M., Anghinolfi, M., et al. 2017, ApJL, 850, L35
Blumenthal, G. R., & Gould, R. J. 1970, RvMP, 42, 237
Bromberg, O., Nakar, E., Piran, T., & Sari, R. 2011, ApJ, 740, 100
Cerenkov Telescope Array Consortium, Acharya, B. S., Agudo, I., et al. 2019,
    in Science with the Cherenkov Telescope Array, ed. CTA Consortium
    (Singapore: World Scientific)
Coppi, P. S., & Blandford, R. D. 1990, MNRAS, 245, 453
Coulter, D. A., Foley, R. J., Kilpatrick, C. D., et al. 2017, Sci, 358, 1556
Dainotti, M. G., Cardone, V. F., & Capozziello, S. 2008, MNRAS, 391, L79
Dainotti, M. G., Willingale, R., Capozziello, S., Fabrizio Cardone, V., &
    Ostrowski, M. 2010, ApJL, 722, L215
Dermer, C. D., & Menon, G. 2009, High Energy Radiation from Black Holes:
    Gamma Rays, Cosmic Rays, and Neutrinos (Princeton, NJ: Princeton Univ.
    Press)
Evans, P. A., Cenko, S. B., Kennea, J. A., Emery, S. W. K., et al. 2017, Sci,
    358, 1565
Fang, K., & Metzger, B. D. 2017, ApJ, 849, 153
Finke, J. D., Dermer, C. D., & Böttcher, M. 2008, ApJ, 686, 181
Fujibayashi, S., Kiuchi, K., Nishimura, N., Sekiguchi, Y., & Shibata, M. 2018,
    ApJ, 860, 64
Gao, H., Zhang, B., Wu, X.-F., & Dai, Z.-G. 2013, PhRvD, 88, 043010
Ghirlanda, G., Salafia, O. S., Paragi, Z., et al. 2019, Sci, 363, 968
Ghisellini, G., Ghirlanda, G., Nava, L., & Firmani, C. 2007, ApJL, 658, L75
Gompertz, B. P., O'Brien, P. T., & Wynn, G. A. 2014, MNRAS, 438, 240
Gottlieb, O., Nakar, E., & Piran, T. 2018a, MNRAS, 473, 576
Gottlieb, O., Nakar, E., Piran, T., & Hotokezaka, K. 2018b, MNRAS, 479, 588
Hamidani, H., Kiuchi, K., & Ioka, K. 2019, arXiv:1909.05867
Hotokezaka, K., Wanajo, S., Tanaka, M., et al. 2016, MNRAS, 459, 35
Ioka, K., Kobayashi, S., & Zhang, B. 2005, ApJ, 631, 429
Ioka, K., & Nakamura, T. 2018, PTEP, 2018, 043E02
Ioka, K., & Nakamura, T. 2019, MNRAS, 487, 4884
Kagawa, Y., Yonetoku, D., Sawano, T., et al. 2015, ApJ, 811, 4
Kagawa, Y., Yonetoku, D., Sawano, T., et al. 2019, ApJ, 877, 147
Kaneko, Y., Bostancı, Z. F., Göğüş, E., & Lin, L. 2015, MNRAS, 452, 824
Kasen, D., Metzger, B., Barnes, J., Quataert, E., & Ramirez-Ruiz, E. 2017,
    Natur, 551, 80
Kasliwal, M. M., Nakar, E., Singer, L. P., Kaplan, D. L., et al. 2017, Sci,
    358, 1559
Kimura, S. S., Murase, K., Bartos, I., et al. 2018, PhRvD, 98, 043020
Kimura, S. S., Murase, K., Mészáros, P., & Kiuchi, K. 2017, ApJL, 848, L4
Kisaka, S., & Ioka, K. 2015, ApJL, 804, L16
Kisaka, S., Ioka, K., Kashiyama, K., & Nakamura, T. 2018, ApJ, 867, 39
Kisaka, S., Ioka, K., & Nakamura, T. 2015, ApJL, 809, L8
Kisaka, S., Ioka, K., & Sakamoto, T. 2017, ApJ, 846, 142
Korobkin, O., Rosswog, S., Arcones, A., & Winteler, C. 2012, MNRAS,
    426, 1940
Kyutoku, K., Ioka, K., & Shibata, M. 2014, MNRAS, 437, L6
Lamb, G. P., Lyman, J. D., Levan, A. J., et al. 2019a, ApJL, 870, L15

Lamb, G. P., Tanvir, N. R., Levan, A. J., et al. 2019b, ApJ, 883, 48
Lazzati, D., López-Cámara, D., Cantiello, M., et al. 2017, ApJL, 848, L6
Lazzati, D., Perna, R., Morsony, B. J., et al. 2018, PhRvL, 120, 241103
Lipunov, V. M., Gorbovskoy, E., Kornilov, V. G., et al. 2017, ApJL, 850, L1
Lyman, J. D., Lamb, G. P., Levan, A. J., et al. 2018, NatAs, 2, 751
Margutti, R., Alexander, K. D., Xie, X., et al. 2018, ApJL, 856, L18
Matsumoto, T., & Kimura, S. S. 2018, ApJL, 866, L16
McKinney, J. C., & Uzdensky, D. A. 2012, MNRAS, 419, 573
Mészáros, P., & Rees, M. J. 2001, ApJL, 556, L37
Metzger, B. D., Quataert, E., & Thompson, T. A. 2008, MNRAS, 385, 1455
Metzger, B. D., Thompson, T. A., & Quataert, E. 2018, ApJ, 856, 101
Mizuta, A., & Ioka, K. 2013, ApJ, 777, 162
Mooley, K. P., Deller, A. T., Gottlieb, O., et al. 2018a, Natur, 561, 355
Mooley, K. P., Frail, D. A., Dobie, D., et al. 2018b, ApJL, 868, L11
Murase, K., Beacom, J. F., & Takami, H. 2012, JCAP, 2012, 030
Murase, K., & Ioka, K. 2013, PhRvL, 111, 121102
Murase, K., & Nagataki, S. 2006, PhRvL, 97, 051101
Murase, K., Toma, K., Yamazaki, R., & Mészáros, P. 2011, ApJ, 732, 77
Murase, K., Toomey, M. W., Fang, K., et al. 2018, ApJ, 854, 60
Murguia-Berthier, A., Montes, G., Ramirez-Ruiz, E., De Colle, F., &
    Lee, W. H. 2014, ApJL, 788, L8
Murguia-Berthier, A., Ramirez-Ruiz, E., Kilpatrick, C. D., et al. 2017, ApJL,
    848, L34
Nagakura, H., Hotokezaka, K., Sekiguchi, Y., Shibata, M., & Ioka, K. 2014,
    ApJL, 784, L28
Norris, J. P., & Bonnell, J. T. 2006, ApJ, 643, 266
Perna, R., Armitage, P. J., & Zhang, B. 2006, ApJL, 636, L29
Pian, E., D'Avanzo, P., Benetti, S., Branchesi, M., et al. 2017, Natur, 551, 67
Ramirez-Ruiz, E., Celotti, A., & Rees, M. J. 2002, MNRAS, 337, 1349
Rees, M. J., & Meszaros, P. 1994, ApJL, 430, L93
Rowlinson, A., O'Brien, P. T., Metzger, B. D., Tanvir, N. R., & Levan, A. J.
    2013, MNRAS, 430, 1061
Sakamoto, T., Barthelmy, S. D., Baumgartner, W. H., et al. 2011, ApJS, 195, 2
Shibata, M., Fujibayashi, S., Hotokezaka, K., et al. 2017, PhRvD, 96, 123012
Shoemaker, I. M., & Murase, K. 2018, PhRvD, 97, 083013
Smartt, S. J., Chen, T.-W., Jerkstrand, A., Coughlin, M., et al. 2017, Natur,
    551, 75
Soares-Santos, M., Holz, D. E., Annis, J., Chornock, R., et al. 2017, ApJL,
    848, L16
Tanaka, M., Utsumi, Y., Mazzali, P. A., Tominaga, N., et al. 2017, PASJ,
    69, 102
Tanvir, N. R., Levan, A. J., González-Fernández, C., et al. 2017, ApJL,
    848, L27
Toma, K., Wu, X.-F., & Mészáros, P. 2009, ApJ, 707, 1404
Troja, E., Piro, L., Ryan, G., et al. 2018a, MNRAS, 478, L18
Troja, E., Ryan, G., Piro, L., et al. 2018b, NatCo, 9, 4089
Utsumi, Y., Tanaka, M., Tominaga, N., Yoshida, M., et al. 2017, PASJ,
    69, 101
Valenti, S., Sand, D. J., Stritzinger, M., et al. 2017, ApJL, 848, L24
Veres, P., & Mészáros, P. 2014, ApJ, 787, 168
Xie, X., Zrake, J., & MacFadyen, A. 2018, ApJ, 863, 58
Xue, Y. Q., Zheng, X. C., Li, Y., et al. 2019, Natur, 568, 198
Zdziarski, A. A. 1988, ApJ, 335, 786
Zhang, B. 2019, FrPhy, 14, 64402